

# Trigger Level Analysis

Andrew James Strange

School of Physics and Astronomy



The University of Manchester

2017 September

A thesis submitted to the University of Manchester  
for the degree of Master of Science  
in the Faculty of Engineering and Physical Sciences

# CONTENTS

<b>Contents</b>	<b>ii</b>
<b>Declaration</b>	<b>iv</b>
<b>Acknowledgements</b>	<b>v</b>
<b>1 Theory</b>	<b>1</b>
1.1 Standard Model . . . . .	1
1.2 Physics of $pp$ Collisions . . . . .	5
1.3 The Higgs Boson . . . . .	8
<b>2 Detector</b>	<b>12</b>
2.1 The Large Hadron Collider . . . . .	12
2.2 The ATLAS Detector . . . . .	13
2.3 Triggers . . . . .	16
2.4 Event Selection . . . . .	18
2.5 Object Reconstruction . . . . .	18
2.6 $b$ -Tagging . . . . .	20
2.7 Trigger-Object Level Analysis . . . . .	22
<b>3 Event Selection</b>	<b>23</b>
3.1 Samples . . . . .	23
3.2 VBF $H \rightarrow b\bar{b}$ Analysis Strategy . . . . .	24
3.3 Jet Extraction . . . . .	24
3.4 Jet Assignment . . . . .	25
3.5 Events . . . . .	25
3.6 Offline Jets . . . . .	25
3.7 Online Jets . . . . .	25
3.8 Offline $b$ -jets . . . . .	25
3.9 Online $b$ -jets . . . . .	26
<b>4 Object Performance</b>	<b>27</b>
4.1 Leading $b$ -jets . . . . .	28
4.2 Leading Non $b$ -jets . . . . .	30
4.3 Jet Tagging Efficiency . . . . .	32
<b>5 Kinematics</b>	<b>35</b>
5.1 Specific Jet Feature Distributions . . . . .	35

5.2	BDT Input Variables . . . . .	35
5.3	Mbb Distribution . . . . .	36
	<b>Bibliography</b>	<b>40</b>

## DECLARATION

This is the declaration. This is not too long, honest!

## ACKNOWLEDGEMENTS

These are the acknowledgements.

## THEORY

## 1.1 Standard Model

The Standard Model (SM) of particle physics is a collection of several theories which provide the most accurate theoretical framework for describing all known components of matter and their interactions to date. The model describes three fundamental forces, each mediated by an integer spin particle called a *gauge boson*, that control interactions between the spin- $\frac{1}{2}$  *quarks* and *leptons* that compose all matter. The framework is comprised of quantum field theories where each particle is an excitation of a corresponding field, and the interactions of the fields govern the particle interactions. The mathematical structure is based on the symmetry group  $SU(3)_c \times SU(2)_L \times U(1)_\gamma$  and is required to be gauge-invariant. The SM does not include gravity as gravitational interactions are significantly weaker than the other fundamental forces (Table 1.3), so are neglected hereafter.

### 1.1.1 Fermions

The full set of spin- $\frac{1}{2}$  *fermions*, described in Tables 1.1 and 1.2, is the combination of the quark and lepton families, which each have three generations. For each distinct particle there is a paired anti-particle which is identical aside from opposite charge and handedness. Most observable matter consists of the first generation of the up and down quarks, the electron and the electron neutrino. Both the leptons and the quarks obey Fermi-Dirac statistics, with quarks experiencing all three fundamental forces, charged leptons interacting via the electromagnetic and weak interactions and neutral leptons experiencing only the weak interaction.

**Table 1.1:** Spin- $\frac{1}{2}$  fermions: quarks  $q$  [1]

Generation	Flavour	Charge / $e$	Mass / GeV
1	Up $u$	+2/3	0.002
	Down $d$	-1/3	0.005
2	Charm $c$	+2/3	1.28
	Strange $s$	-1/3	0.096
3	Top $t$	+2/3	173.1
	Bottom $b$	-1/3	4.18

**Table 1.2:** Spin- $\frac{1}{2}$  fermions: leptons  $l$  [1]

Generation	Flavour	Charge / $e$	Mass / MeV
1	Electron $e$	-1	0.511
	Electron Neutrino $\nu_e$	0	$\sim 0$
2	Muon $\mu$	-1	105.658
	Muon Neutrino $\nu_\mu$	0	$\sim 0$
3	Tau $\tau$	-1	1776.86
	Tau Neutrino $\nu_\tau$	0	$\sim 0$

Quarks are always confined into colour singlet *hadrons* bound by the strong interaction, which are either *baryons* ( $qqq$ ) like the *proton* ( $uud$ ) and *neutron* ( $ddu$ ), or *mesons* ( $q\bar{q}$ ) like the positive *pion* ( $u\bar{d}$ ). When a high energy hadron is produced, the interaction of the strong force on the quarks results in a collimated *jet* of hadrons that freeze out of the initial hadron. This process is described in more detail in Section 1.2.2.3.

### 1.1.2 Forces

All forces arise due to the exchange of unobservable virtual particles, gauge bosons, which obey Bose-Einstein statistics. The three fundamental particle interactive forces for the SM are named the strong, weak and electromagnetic interactions, and are mediated by *gluons*, *weak bosons* and *photons* respectively. The gauge bosons are described in more detail in Table 1.3. In addition to the forces, particles acquire mass by coupling to the *Higgs* field via the spin-0 Higgs boson [2–4], which is covered in more detail in Section 1.1.3.

**Table 1.3:** Spin-1 gauge bosons. The strength of the interaction is typically stated in terms of  $\alpha$ , a dimensionless constant proportional to the matrix element for the virtual particle exchange for each interaction. The weak interaction is intrinsically stronger than the EM interaction, but the mass of the weak bosons limits the range to extremely short distances. The strength of gravity is  $\sim 10^{-39}$  hence it is neglected. [1]

Interaction	Particle	Charge / $e$	Mass / GeV	Strength ( $\alpha$ )
Strong	Gluon $g$	0	0	$\sim 1$
Weak (Charged Current)	$W^+$	1	80.4	$10^{-6}$
	$W^-$	-1	80.4	
Weak (Neutral Current)	$Z$	0	91.2	
Electromagnetic (EM)	Photon $\gamma$	0	0	$\frac{1}{137}$

### 1.1.2.1 Quantum Chromodynamics

Quantum Chromodynamics (QCD) is the theory of the strong interaction, mediated by the gluon which couples to colour charge. It corresponds to the  $SU(3)_c$  symmetry group of the overall SM. The strong interaction conserves energy, momentum, angular momentum and colour charge. Only quarks and gluons themselves possess colour charge, so while quarks are the only fermion to feel the strong interaction, gluons can self-couple.

### 1.1.2.2 Electroweak Unification

Electroweak Unification (EW) is the expression of the electromagnetic interaction and the weak interaction as separate manifestations of a combined electroweak force in the Glashow-Weinberg-Salam model [5–7], which corresponds to the  $SU(2)_L \times U(1)_Y$  symmetry group. Quantum Electrodynamics (QED) describes the macroscopically observable  $U(1)$  electromagnetic force with the photon as the mediating boson, and any interaction conserves energy, momentum, parity and charge and additionally never changes particle type through the interaction. The  $SU(2)$  weak interaction is mediated by the charged current vector bosons  $W^+$ ,  $W^-$  and the neutral current vector boson  $Z$ , which have large masses that limit the weak interaction to very short distances. The charged current interaction is capable of changing the flavour of a particle and also of violating parity in an interaction.

The weak interaction by itself was observed to diverge from observation at high energies, leading to the introduction of the unified theory. The combined  $SU(2)_L \times U(1)_Y$  group produces four gauge bosons which mix to produce the more recognisable  $\gamma$ ,  $W^+$ ,  $W^-$  and  $Z$  bosons. The unified force couples to weak isospin, which allows self-coupling between the massive vector bosons, but not the photon as it does not carry electric charge.

While the weak interaction acts on both quarks and leptons, the quark sector is affected by



the distinction between the mass and flavour eigenstates of quarks. The physically observed flavour eigenstates are distinct from the quark eigenstates of the weak interactions, which are superpositions of the mass eigenstates. The effect of this quark mixing in the weak interaction is that different flavour changing interactions have different strengths. The mixing of the mass eigenstates ( $q$ ) into weak eigenstates ( $q'$ ) is described by the Cabbibo-Kobayashi-Makasawa matrix [8, 9]:

$$\begin{pmatrix} d' \\ s' \\ b' \end{pmatrix} = \begin{pmatrix} V_{ud} & V_{us} & V_{ub} \\ V_{cd} & V_{cs} & V_{cb} \\ V_{td} & V_{ts} & V_{tb} \end{pmatrix} \begin{pmatrix} d \\ s \\ b \end{pmatrix} \quad (1.1)$$

### 1.1.3 Spontaneous Symmetry Breaking: The Higgs Boson

The gauge field theories used for the QCD and EW models when unaltered require massless gauge bosons in order to preserve gauge invariance, which follows from the Klein-Gordon equation:

$$\frac{\partial^2 \psi}{\partial t^2} = (\nabla^2 - m^2) \psi \quad (1.2)$$

This is satisfactory for the gluon and photon, but a separate theory is required to explain the mass of the  $W^\pm$  and  $Z$  bosons. The Higgs Mechanism proposed introducing a scalar field that interacts with the  $W^\pm$  and  $Z$  fields. In the Lagrangian formulation this results in a term akin to a mass term ( $\propto \psi^2$ ) which effectively links that mass of the bosons to their coupling with this scalar field. This addition to the Lagrangian is still required to preserve the symmetry of the system and respect the gauge invariance, but is also required to have a non-zero expectation value for the field in the vacuum or ground state of space. The Higgs mechanism introduces the scalar field  $\phi$  which has a potential energy  $V(\phi)$ :

$$V(\phi) = a\phi^4 - b\phi^2 \quad (1.3)$$

This results in an equilibrium point ( $\phi = 0$ ) that respects the symmetry, but is inherently unstable, with an infinite set of degenerate non-zero minima at  $|\phi^2| = \frac{b}{2a}$  where the symmetry is *spontaneously* broken. This field, in an analogous fashion to the other quantum fields of the SM, can produce particles from excitations which form the physical *Higgs Scalar Boson*  $H$ . Confirmation of the Higgs boson as part of the SM was only achieved relatively recently [10, 11], where a spin-0 boson consistent with the SM Higgs was observed. Subsequent measurements made have provided agreement on the new particle as the Higgs boson with a mass of 125.09 GeV [1]. Section 1.3 covers in more detail the production and behaviour of the Higgs boson in collider experiments.

## 1.2 Physics of $pp$ Collisions

Recent experimental efforts to probe the Standard Model have focused on high-energy collider experiments, where beams of particle with equal energy are collided head on within detectors. For proton-proton ( $pp$ ) collisions, matters are complicated as the colliding protons are composite particles, which at high energy consist of the three *valence* quarks and a sea of virtual quarks and gluons. Collectively these constituents are referred to as *partons* where each parton carries a fraction of the overall hadron momentum, and the interaction in the  $pp$  collision consists of elastic scattering between these partons. At a given energy scale  $Q^2$  the probability that a parton  $i$  carries a fraction  $x_i$  of the overall momentum is described by the parton distribution function (PDF)  $f_i(x, Q^2)$ . These PDFs cannot be calculated from QCD but can be determined from experimental measurements, and collections of PDFs have been assembled from the leading collider experiments [12].

In any particle interaction, the probability a particular reaction occurs is in proportion to the cross section of the reaction. The cross section for a short range, hard parton-parton collision is given by  $\hat{\sigma}(Q^2)$ , where scattering energy scale  $Q^2 = x_1 x_2 E_{cm}^2$  in the parton-parton centre-of-mass frame where  $E_{cm}$  is the energy in the centre-of-mass frame. To compute the cross section  $\sigma$  for some hard process  $pp \rightarrow X$ , all possible combinations of incoming partons must be summed over and the momentum fractions integrated over while accounting for the PDFs:

$$\sigma = \sum_{i,j=q,g} \int dx_1 dx_2 f_i(x_1, Q^2) f_j(x_2, Q^2) \hat{\sigma}(Q^2) \quad (1.4)$$

### 1.2.1 Geometry

The high energy protons used in collisions are relativistic in nature, and as the momenta of the colliding partons are not guaranteed to be equal and opposing there is always an unknown element of longitudinal boosting in  $pp$  collisions. As a consequence, use of light-cone coordinates and some definitions of convenient quantities can be of benefit to  $pp$  collision analyses [13].

Typically the momentum in the transverse plane  $p_T$  is used for a particle, and the rapidity  $y$  of a particle with non-zero  $p_T$  is defined:

$$y = \frac{1}{2} \ln \frac{E + p_z}{E - p_z} \quad (1.5)$$

This rapidity  $y$  transforms additively to boosts along the  $z$  axis, so any rapidity difference between two objects is invariant to such boosts. For cases where the mass of a particle is negligible (highly relativistic particles) the rapidity can be related to the polar angle of the particle as the pseudo-rapidity  $\eta$ :

$$\eta = -\ln \tan \frac{\theta}{2} \quad (1.6)$$

The distance between two objects within the detector is commonly expressed in the  $(\eta, \phi)$  space rather than absolute, with this separation being given by  $\Delta R = \sqrt{(\Delta\eta)^2 + (\Delta\phi)^2}$

### 1.2.2 Collision simulation

A  $pp$  collision is a complex event which results in a significant number ( $\mathcal{O}(1000)$ ) of final state particles, each of which interact and evolve over the timescale of an event. This progression of the collision event can be broken down into distinct stages of behaviour of the produced particles: the *hard process*, *parton shower*, *hadronisation*, *unstable particle decays* and *underlying event*.

This breakdown is key to the simulation of  $pp$  collisions using Monte-Carlo event generators, the use of which is critical in current high energy physics research. Monte-Carlo simulations of collisions are used to predict and prepare for real data-taking experiments, obtain control datasets of particular particle interactions and act as controls to optimise analysis tools. The breakdown of the interaction into distinct stages has allowed specialised software to be produced for each step, which makes use of a characteristic scale and certain safe approximations for the step to provide reliable predictions, while reducing the computational demands of the simulation [14].

#### 1.2.2.1 Hard Process

The first stage of a  $pp$  collision and the first step of a simulation, the hard scatter refers to highest momentum transfer process in the event between coloured particles, and forms the core of the event. This details the interaction of partons entering the event and those outgoing partons resulting from the process. In simulation the probability distribution of the partons is calculated from perturbation theory to the desired accuracy (LO, NLO etc) using the PDFs of the constituents.

#### 1.2.2.2 Parton Shower

While the hard scatter interaction in a collision is relatively straightforward, the overall behaviour of the partons is much more complex as they progress through the event. The incoming and outgoing partons from the hard scatter radiate additional interaction particles during the event. The Bremsstrahlung radiation of photons by scattered electric charges is well described by QED, and the analogous radiation of gluons by scattered colour charges as explained by QCD produces additional partons within the interaction. However, as the gluons produced by QCD scattering themselves carry colour charge, there is extending showering of gluons producing gluons, resulting in the phase space of the interaction being filled with a sea of soft gluons. Both of these radiative processes make up the parton shower stage of the event simulation.

The evolution of these parton showers is evaluated in Monte-Carlo simulations using a step-by-step iterative process, on the scale of momentum transfer in the interaction. This process is started at the hard scatter and evolved through the interaction with decreasing momentum scale until the point at which perturbation theory breaks down, necessitating a different evaluation method.

### 1.2.2.3 Hadronisation

With the breakdown of perturbation theory at low momentum scales, observable colourless hadrons are constructed from the coloured partons using hadronisation models in order to extend the simulation. These hadrons are the physical final state particles observed in the detector, which exist due to the colour confinement of the quarks and gluons. Within a particle detector, rather than individual hadrons *jets* of hadrons are observed. As a coloured fragment produced in the interaction moves away from the interaction, it will create other coloured fragments around itself in order to produce a confined hadron while moving away from the collision. This occurs repeatedly for each hadron ejected from the collision as it moves away, producing a collimated stream of hadrons which make up a jet.

In simulation this step involves collecting the partons produced in the parton shower into hadrons, and is typically evaluated using either a String model [15] or a Cluster model [16]. These steps are models, and not calculations as to how the partons combine, as to calculations being prohibited by the breakdown of perturbation theory.

### 1.2.2.4 Unstable Particle Decays

The final stage of the evolution of the parton shower considers the hadrons produced during the shower. These hadrons may not be stable particles but could be resonances that go on to decay within the detector to produce the more stable hadrons observed in the data. Most modern simulation software models these decays, but the exact specification of the decay tables and channels has a significant impact on the final state of the simulation.

### 1.2.2.5 Underlying Event

While the hard scatter and subsequent parton shower results from the highest momentum interaction of the  $pp$  collision, the remnants of the proton not involved in this will continue to interact with each other. This produces additional soft hadrons that fill the interaction environment, overlapping with the products of the hard scatter interaction.

The dominant model for simulation of the underlying event is a perturbative model where the other components undergo additional discrete hard scatter interactions and corresponding

parton showers which are simulated in an corresponding fashion to the core scattering.

### 1.2.3 Monte-Carlo Software

There is a broad selection of software tools for evaluating  $pp$  collisions, from general purpose simulations like PYTHIA [17] or SHERPA [18] which are used to evaluate the complete process, to more specific tools like POWHEG [19] which is used to produce hard scatter events with NLO matrix elements. Most software packages make use of the chain of generation for an event outlined previously, and modern analyses will make use of multiple generators interfaced together to compute different steps with improved accuracy.

## 1.3 The Higgs Boson

Detecting the SM Higgs boson is strongly dependent on the predominant production and decay channels for the Higgs boson, which in turn depend on the specifications of the collider used for the search. In this section the relevant production and decay channels at the Large Hadron Collider (LHC) will be discussed.

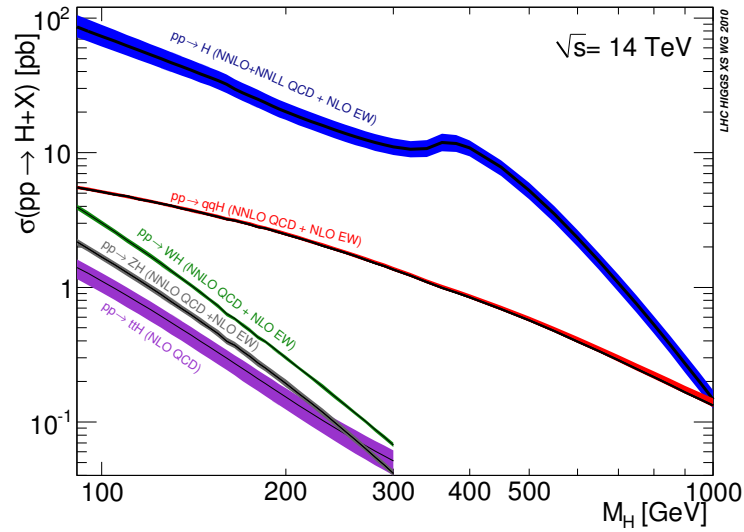


**Figure 1.1:** SM Higgs Production cross section for  $\sqrt{s} = 14$  TeV.  $pp \rightarrow H$  corresponds to gluon-gluon fusion production and  $pp \rightarrow qqH$  vector boson fusion. [20]

### 1.3.1 Higgs Production

While there are many various methods for production of a Higgs boson, at the LHC the cross section is dominated by gluon-gluon fusion ( $gg \rightarrow H$ ) as shown in Figure 1.1, with the

second largest cross-section arising from Vector Boson Fusion (VBF, Section 1.3.2). Other significant production processes are the associated production with a weak boson ( $WH/ZH$ , Higgs-strahlung) production modes and associated production with top quarks ( $t\bar{t}H$ ) [20]. The lowest order Feynmann diagrams for these processes are shown in Figure 1.2.

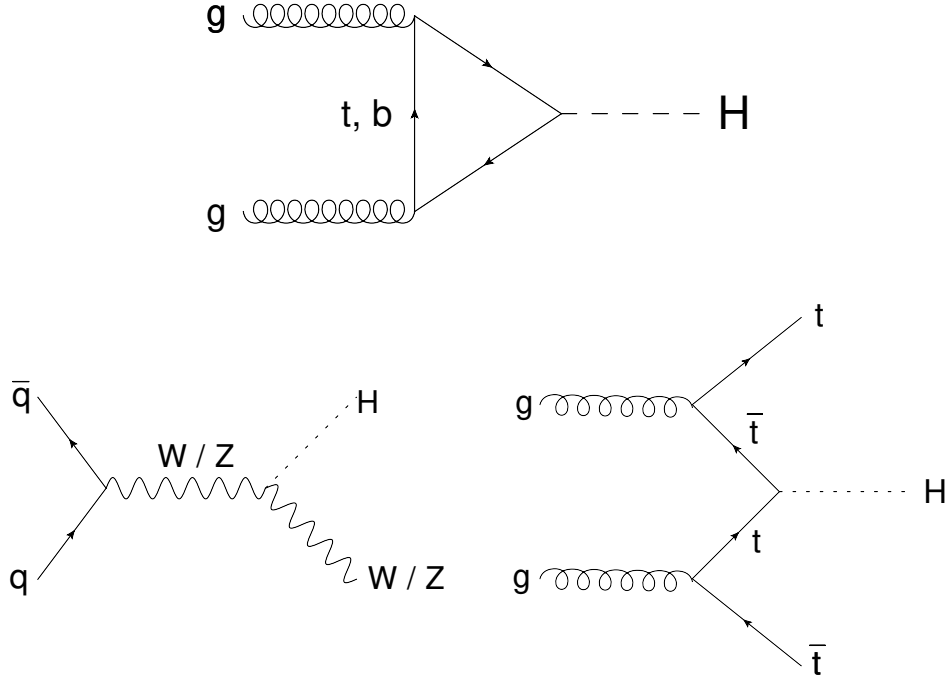


**Figure 1.2:** Lowest order Feynmann diagrams for gluon-gluon fusion ( $gg \rightarrow H$ ),  $W/Z$  associated production ( $WH/ZH$ ) and top anti-top associated production ( $t\bar{t}H$ ).

### 1.3.1.1 Gluon-gluon Fusion

The dominant production mechanism for the Higgs boson in hadron colliders is the  $gg \rightarrow H$  production via an intermediate quark loop. The dynamics of this mechanism are controlled by strong interactions, thus calculations of QCD corrections are necessary for any accurate predictions, and have been computed up from next-to-leading order (NLO) to  $N^3\text{LO}$  for the  $gg \rightarrow H$  process in recent years, along with the inclusion of Electro-Weak corrections in the cross section calculations [20].

### 1.3.2 Vector Boson Fusion

Production of a Higgs boson from the fusion of vector bosons radiated from initial-state quarks is the second largest cross-section at the LHC, and is useful as a production mode due to topological characteristics which can distinguish the event from  $gg \rightarrow H$ . In VBF  $H \rightarrow b\bar{b}$ , the characteristic topology is a pair of central  $b$ -jets forming the Higgs candidate, and two forward,

close to the beam line VBF jets formed from remnants of the initially colliding protons as displayed in Figure 1.3. In addition central jet activity is suppressed due to the lack of colour exchange between the colour single Higgs boson and the decay  $b$ -quarks [21]. These distinct features mean that while the cross section for VBF at a Higgs mass of  $< 200$  GeV is dominated by  $gg \rightarrow H$ , the easy to detect signature means the channel is a cornerstone of searches for the Higgs boson.

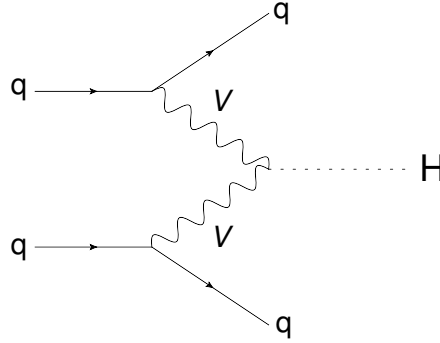


**Figure 1.3:** Feynmann diagram for the production of a Higgs boson via Vector Boson Fusion, where  $q$  denotes any quark or antiquark

### 1.3.3 Higgs Decay

The branching ratios for decays of the Higgs boson in the Standard Model have been extensively determined using Monte-Carlo event generators. As is to be expected, the relative cross-sections of the decay modes are strongly dependent on the mass of the Higgs boson, as highlighted in Figure 1.4.

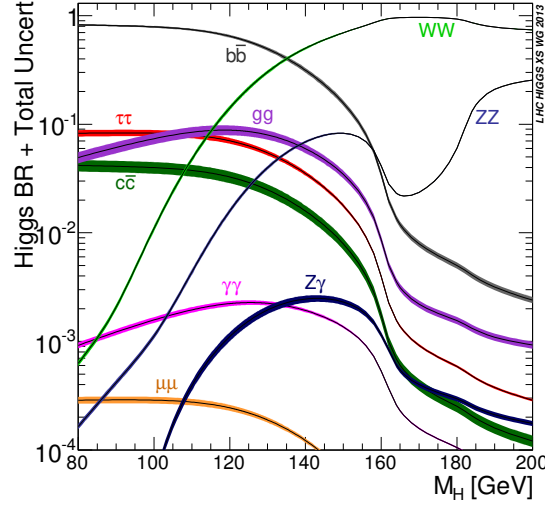


**Figure 1.4:** Higgs decay branching ratios for the low mass region with their uncertainties [22].

While observations consistent with the Standard Model Higgs boson have been made for the  $H \rightarrow \gamma\gamma$ ,  $H \rightarrow ZZ$ ,  $H \rightarrow W^+W^-$  and  $H \rightarrow \tau^+\tau^-$  channels, observation of the  $H \rightarrow b\bar{b}$  decay channel is significantly hindered owing to the large background from multijet production in hadron collisions. Despite this, the topology of the VBF production mechanism makes it a viable option for observation of the  $b\bar{b}$  decay channel.

### 1.3.4 VBF Searches

Searches for the VBF  $H \rightarrow b\bar{b}$  interaction look for a resonance in the invariant mass of a pair of jets containing  $b$ -quarks ( $m_{bb}$ ) in events with the characteristic topology. This characteristic topology distinguishes the signal events from the multijet events that form the dominant background with a non-resonant  $m_{bb}$  spectrum. An additional resonant background contribution to the spectrum is due to decay of a  $Z$  boson to two jets in association with two jets.

In the most recent searches for the Higgs boson produced via VBF, which this analysis emulates, the VBF  $H \rightarrow b\bar{b}$  events are indistinguishable from the  $gg \rightarrow H$  events, and are separated using a multivariate boosted decision tree (BDT) analysis to refine the phase space to the most VBF sensitive BDT regions.



## 2.1 The Large Hadron Collider

The Large Hadron Collider (LHC) is a circular particle accelerator operated at European Organisation for Nuclear Research (CERN, Conseil Européen pour la Recherche nucléaire). Currently the largest accelerator in the world, the LHC is designed to collide heavy ions or opposing proton beams for a peak design *centre-of-mass energy*  $\sqrt{s} = 14\text{TeV}$  with a luminosity of  $10^{34}\text{cm}^{-2}\text{s}^{-1}$  [23]. The first proton beams were circulated in the LHC in 2008, with Run-1 of LHC data taking being conducted until 2013, at which point the machine was shut down for maintenance. Following on from the initial operations, Run-2 of the LHC has been ongoing since 2015, operating at  $\sqrt{s} = 13\text{TeV}$ .

The principle LHC ring consists of eight pairs of alternating long arc sections and short straight insertion sections, situated within the underground tunnel excavated for the older Large Electron Positron Collider experiment [24, 25]. The arc sections contain the dipole magnets used to bend the particle beam around the ring, while the straight sections contain four interaction points, at each of which the large experiments are located. The remaining straight sections contain the operational systems of the LHC: beam acceleration, injection, dumping and collimation. The proton beams are generated outside the principle ring and inserted into the ring by the LHC injector chain, a sequence of smaller accelerators which are used to bring the proton beams up to a suitable energy for injection. The proton beams injected into the accelerator originate from a cloud of hydrogen gas, which is passed through an electric field to strip the electrons before the protons are inserted into the beam acceleration components. The proton

beams are arranged such that the protons move in bunches of  $O(10^{11})$  protons, with multiple bunches placed into trains. During Run-2 the LHC operated with bunch spacings between the bunch trains of 50ns and 25ns.

The principle measure of the operation of the LHC is the beam *luminosity*, expressed as either an instantaneous luminosity  $L$  or an integrated luminosity. This parameter is a measure of the rate of collisions within the accelerator, given by:

$$L = \frac{1}{\sigma} \frac{dN}{dt} = \frac{n_b n_1 n_2 f}{2\pi \Sigma_x \Sigma_y} \quad (2.1)$$

where in the general case  $\sigma$  is the interaction cross section and  $\frac{dN}{dt}$  is the event rate. In the LHC specific formula,  $n_b$ ,  $n_1$  and  $n_2$  are the number of bunch crossing producing collisions, and the number of bunches in both of the colliding beams,  $f$  the machine revolution frequency, and  $\Sigma_{x,y}$  are parameters relating to the beam width. This instantaneous luminosity is integrated across a time period, such as an LHC Run or a specific data period, to produce the integrated luminosity  $\int L dt$  which corresponds to the available data to analyse.

Once a beam is accelerated to the target energy collisions begin at the interaction points. Interactions are ongoing for periods of several hours, and will go on until the the beam is replaced due to general decay of the interaction rate or beam instabilities.

At the LHC, the four large experiments at the interaction points are ATLAS (A Toroidal LHC ApparatuS), CMS (Compact Muon Solenoid), LHCb (LHC beauty) and ALICE (A Large Ion Collider Experiment). LHCb is a forward spectrometer heavy flavour experiment, designed to study flavour physics with emphasis on the  $b$ -quark and on matter/anti-matter asymmetry. ALICE focuses on the collisions of heavy ions, while ATLAS and CMS are general purpose detectors to conduct experiments across a broad range of modern physics research areas.

### 2.1.1 Run Conditions in 2016

Over the course of 2016, following beam commissioning runs, the LHC beam was operated predominantly with two beams of energy 6.5TeV for  $\sqrt{s} = 13\text{TeV}$ . Over the course of the 2016 data-taking the ATLAS and CMS experiments achieved an integrated luminosity of  $40 \text{ fb}^{-1}$  with a peak instantaneous luminosity of  $1.4 \times 10^{34} \text{ cm}^{-2} \text{ s}^{-1}$  with 2220 bunches per beam [26].

## 2.2 The ATLAS Detector

The ATLAS detector [27] is a multi-purpose detector designed to study a broad selection of physics phenomena within the experimental conditions of the LHC. The detector is cylindrical in structure with the axis aligned to the beam path and nominally forward-backward symmetric

in terms of the beam collision point at the centre of the detector. The detector provides approximately  $4\pi$  solid angle coverage around the interaction point to detect as many collision products as possible.

The structure of the ATLAS detector is composed of concentric subsystems around the interaction point. The Inner Detector (ID) is the component closest to the interaction point, and is contained in a superconducting solenoid. This is surrounded by high-granularity calorimeters and an extensive muon spectrometer contained within and eight-fold azimuthally symmetric arrangement of three large toroidal magnets. A schematic representation of the ATLAS detector is shown in Figure 2.1. The subsystems are arranged into three cryostats, two *endcaps* located on the ends of the detector and the central *barrel* section. Discussion of the coordinates and quantities used in the detector is found in Section 1.2.1. A summary of the operational parameters of the principle detector components is given in Table 2.1.

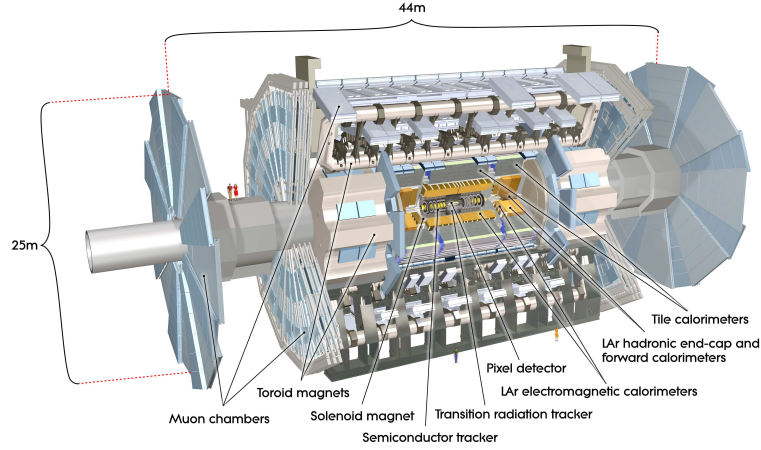


**Figure 2.1:** Schematic cut-away of the ATLAS detector [28].

### 2.2.1 Inner Detector

The Inner Detector provides pattern recognition, momentum measurements, electron identification and measurements of both primary and secondary vertices to efficiently identify jets containing  $b$ -hadron within a pseudorapidity range  $|\eta| < 2.5$ . The ID itself is contained within a 2 T solenoidal field, which is used to bend the paths of charged particles within the ID. The ID is specifically designed to have a high momentum resolution (Table 2.1), and consists of three separate detector sections: the silicon pixel detector provides fine granularity track and vertex reconstruction, the silicon strip semiconductor tracker measures the trajectory of transiting charged particles and the outer transition radiation tracker used for particle identification is comprised of layers of straw tubes containing mixtures of xenon, oxygen and carbon dioxide.

### 2.2.2 Calorimeters

Calorimeters are used to measure the energy of any particle moving out from the interaction point. These particles cause the development of either Electromagnetic (EM) or hadronic showers within the calorimeter substrate, and the energy deposited in this shower can be used to calculate the energy of the incoming particle. The ATLAS calorimetry system consists of a combination of EM and hadronic calorimeters arranged with full  $\phi$ -symmetry around the beam axis. The combination of all separate calorimeters provides pseudorapidity coverage in the range  $|\eta| < 4.9$ . Within the pseudorapidity region of the inner detector, the fine granularity of EM calorimeters is optimised for measurements of electron and photon tracks and momenta, while the coarser hadronic calorimeters contained in the remainder of the calorimeter system are sufficient for jet reconstruction and missing energy calculations. The structure and design of the calorimeter components has been optimised to provide complete azimuthal coverage, take into account the engineering requirements for assembling the detector for desired calorimetry performance and account for radiation considerations between the different detector components [27].

The EM calorimeter is a lead-Liquid-Argon (LAr) detector, which is split into a barrel section (EMB,  $|\eta| < 1.475$ ) and two endcap sections (EMEC,  $1.375 < |\eta| < 3.2$ ) with each section contained in a separate cryostat. The EMB consists of two identical half-barrels split by a small gap at  $z = 0$ . Each of the EMEC sections is a pair of coaxial wheels, with the inner and outer sections covering regions  $1.375 < |\eta| < 2.5$  and  $2.5 < |\eta| < 3.2$  respectively. The major body of the EM calorimeter is divided into 3 sections of decreasing cell granularity, moving out from the beamline.

Hadronic calorimetry for particles undergoing the strong interaction is provided by the steel/scintillator tile calorimeter, for pseudorapidity values of  $|\eta| < 1.7$ , and by the LAr flat-plate Hadronic Endcap Calorimeter (HEC) for  $1.5 < |\eta| < 3.2$ . The tile calorimeter directly surrounds the EM calorimeter, and is split into a central barrel section for  $|\eta| < 1.0$  and two extended barrel sections covering  $0.8 < |\eta| < 1.7$ . The HEC, akin to the EMEC, consists of two separate wheels per end-cap covering  $1.5 < |\eta| < 3.2$ , and is contained within the same cryostat as the EMEC. The HEC consists of alternating copper plates with LAr gaps to act as the active medium.

In addition to the barrel and end-cap calorimeters, the LAr Forward Calorimeter is contained within the end-cap cryostat (The FCal is omitted from Figure 2.1) and is designed to perform both EM and hadronic calorimetry across a pseudorapidity range of  $3.1 < |\eta| < 4.9$  using a combination of copper/LAr (EM) and tungsten/LAr (hadronic) calorimeter components.

### 2.2.3 Muon Spectrometer

The muon spectrometer is the outermost component of the ATLAS detector, measuring trajectory and momentum of muons from the interactions within a pseudorapidity range of  $|\eta| < 2.7$ . The muon system consists of three large superconducting coils that deflect the muon trajectories. The system is designed for high precision tracking of the minimally ionising muons and for use in the triggering system.

**Table 2.1:** Performance goals and operational ranges for the principle components of the ATLAS detector. [27]

System	Component	$\eta$ Coverage	Resolution
Tracking		$0 <  \eta  < 2.5$	$\sigma_{p_T}/p_T = 0.05\% p_T \oplus 1\%$
EM Calorimetry	EMB	$0 <  \eta  < 1.475$	$\sigma_E/E = 10\%/\sqrt{E} \oplus 0.7\%$
	EMEC (Inner)	$1.375 <  \eta  < 2.5$	
	EMEC (Outer)	$2.5 <  \eta  < 3.2$	
Hadronic Calorimetry	Tile (Barrel)	$0 <  \eta  < 1$	$\sigma_E/E = 50\%/\sqrt{E} \oplus 3\%$
	Tile (Extended)	$0.8 <  \eta  < 1.7$	
	HEC	$1.5 <  \eta  < 3.2$	
Forward Calorimetry	FCal	$3.1 <  \eta  < 4.9$	$\sigma_E/E = 100\%/\sqrt{E} \oplus 10\%$
Muon Spectrometer		$0 <  \eta  < 2.7$	$\sigma_{p_T}/p_T = 10\% \text{ at } p_T = 1 \text{ TeV}$

## 2.3 Triggers

When operating at the design luminosity, the LHC produces a bunch-crossing rate of 40 MHz [29]. This extreme rate of interaction necessitates a trigger system to reduce the output rate to a suitable level for offline processing, which is predominantly limited by the rate at which data can be written to disk. The limit of the output rate is determined by the computational capabilities, specifically the average data rate of output. The trigger system selects events by quickly identifying distinguishing features of events (i.e. signatures of muons, electrons, jet and  $b$ -jet objects) and using combinations of these signatures to signify an event as relevant for further analysis. Overall usage of the trigger system brings the output rate down to 1 kHz with a maximum Level 1 trigger (L1) rate of 100 kHz.

The ATLAS trigger system consists of a chain of selection stages of increasing severity and corresponding decrease in rate. A schematic outline of the trigger system is shown in Figure 2.2. This outline covers both the logical process and the transfer of data between components of the trigger chain. The principle decision logic of the trigger system is however contained in two sections, the L1 trigger system and the High Level Trigger (HLT).

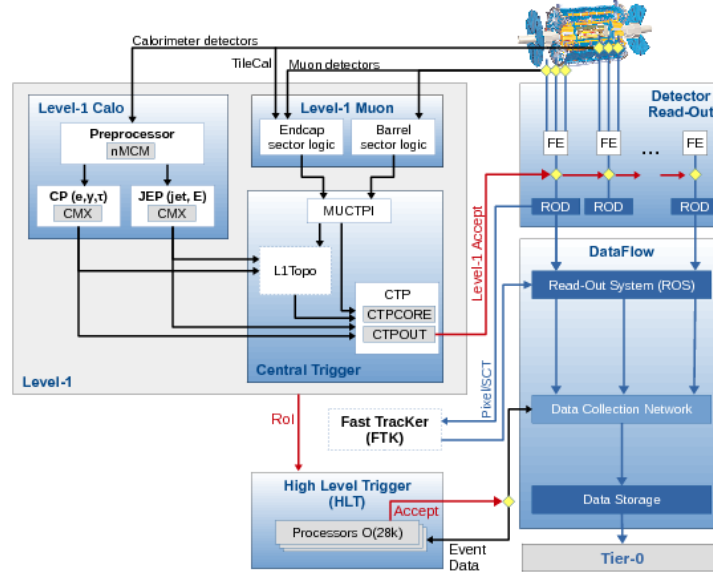


**Figure 2.2:** Schematic plot of the ATLAS Trigger and Data acquisition system [30].

The L1 trigger system [31] is a hardware based decision system, using fast custom electronics to minimise latency in any decision. The L1 uses reduced-granularity data from the calorimetric and muon detectors, reconstructed objects and missing and total transverse energy. The high bunch-crossing rate means instantaneous processing of the event is non-viable, so event readouts are stored in a buffer chain of events to be evaluated with a fixed permitted decision time per event. Along with this first selection, the L1 trigger defines *Regions of Interest* (RoIs) in the phase space within the detector, which are labeled for investigation in the HLT. TALK ABOUT RATE

In contrast to the hardware computation of the L1 system, the HLT consists of software algorithms running in a farm of  $\approx 40000$  interconnected processors [29]. Following acceptance of an event by the L1 trigger, events are transferred from the initial data pipeline to dedicated readout buffers for the HLT. The HLT performs processing on the events using finer-granularity information from the calorimeters and muon spectrometer, along with making use of information from the ID, which is unavailable to L1. This more precise data is then computed using object reconstruction algorithms to generate particle objects similar to the objects reconstructed after the data has been stored. The decision at HLT level to store an event is managed by a trigger chain, which is a sequence of specific criteria and algorithms evaluated on an event in sequence. A key component of the trigger chain is the prescaling factor of the chain. If the particular event requirements are not tight cuts, the overall output rate of the trigger chain is reduced by the prescale factor to bring the output rate within bandwidth limits. The HLT provides  $O(1000)$

independent trigger chains for evaluating events. Along with the partial reconstruction of relevant objects, the HLT is capable of performing complete reconstruction of an event, and also capable of writing out these partial or complete reconstructions of an event into different data streams from the complete detector readout for use in analysis. The standard terminology for events and data recorded and processed during the operation of the LHC is *online* data, while objects and information produced by considering the output of the detector after the data has been stored is termed *offline*. These terms are used extensively throughout the rest of this analysis to distinguish between the different data sources.

## 2.4 Event Selection

Beyond the reduction in event storage handled by the trigger chains and prescaling, only select sections of the overall output dataset are ever used in analyses. The LHC is not free from operational errors or issues with the hardware and software of the detector. Parts of the output data can be corrupted by incomplete events due to detector failings, poor data integrity or disruption of the machine. From the complete output for a Run section, which is divided into luminosity blocks, only the blocks which have been marked as *good* are made use of in analyses. The internal directory of usable luminosity blocks is named the Good Runs List (GRL).

## 2.5 Object Reconstruction

### 2.5.1 Jets

As discussed in Section 1.2.2.3 the coloured fragments produced during collisions produce collimated streams of hadrons called jets, which are the physical objects detected in the event. Detectors make use of algorithms to reconstruct these jets from the calorimeter readouts to relate the stream of hadrons to the initial fragmented partons. There are various algorithms used to reconstruct jets within the ATLAS detector, and these algorithms commonly require the definition of a jet to be invariant under additional soft or collinear emissions. Such algorithms are designated as infra-red (IR) or collinear (C) safe.

Modern jet algorithms are broadly split into cone-type algorithms, which take the hardest (highest momentum) object in an event as a seed of an iterative process of looking for a stable cone rooted at this seed. Once a cone is defined, any constituents contained within the cone are removed from consideration and the process repeats. The alternate method is the sequential clustering algorithm, which assumes that particles within jets will have small differences in transverse momentum and groups particles based on the momentum space to reconstruct the jets. Sequential clustering algorithms function using iterative steps with two distance parameters.

The first distance is the separation between two particles  $d_{ij} = \min(p_{Ti}^a, p_{Tj}^a) \frac{\Delta R_{ij}^2}{R}$ , where  $a$  is a particular exponent for a given algorithm,  $R$  is the radius parameter of the final reconstructed jet size and  $\Delta R_{ij}$  is the  $(\eta, \phi)$  space distance between the two objects. The second parameter,  $d_{iB} = p_{Ti}^a$ , is the momentum space distance between the beam axis and an object [32].

The principle algorithm used for jet reconstruction at ATLAS is the anti- $k_t$  algorithm [33], which is a sequential clustering algorithm with  $a = -2$ . The algorithm is seeded with the highest  $p_T$  particles in the event, and iteratively computes both distance parameters. At each step, the two are compared: if  $d_{ij}$  is smaller, particles  $i$  and  $j$  are combined whereas if  $d_{iB}$  is smaller particle  $j$  is labeled as a jet. The fact this algorithm tends to result in approximately circular reconstructed jet objects makes it favourable for modern analyses. The sequential clustering algorithms are in addition theoretically preferable, but were impractical until recent advancements in the algorithms gave significantly increased computational performance. The anti- $k_t$  algorithm is IRC safe and typical used with  $R = 0.4$  in the ATLAS experiment, and can be readily applied to clustering partons and calorimeter deposits in addition to hadrons.

During jet reconstruction, when the energy deposits are extracted from the calorimeter, there is the option of reading the calorimeter cells according to the Electromagnetic (EM) scale, which is calibrated using test electron beams, or by applying Local Cell (LC) corrections to account for the attenuated physical response of the calorimeter and the difference in hadronic and electromagnetic response, which restores the energy of extracted objects to correspond to Monte-Carlo simulated truth objects. In this analysis, readouts of all jet objects, both offline and trigger level, were taken at the EM energy scale.

### 2.5.1.1 Pileup

As mention in Section 1.2.2.5 on the process of a  $pp$  collision, there are additional significant interactions as a result of the additional parton interactions accompanying the hard-scatter interaction of the collision. These lower  $p_T$  collisions produce additional jets and objects that contaminate the signal collision. The collection of these jets in the detector output is termed in-time pileup. In addition to the jets from the underlying event, interactions from preceding or subsequent bunch crossings also contribute contaminating objects to the detector readout, which is named out-of-time pileup. In-time and out-of-time pileup are collectively referred to as pileup in the detector, and necessitate processing and calibration of the detector output to remove the effects from consideration [34].



### 2.5.2 *b*-Tagging

Identification of *b*-quark jets in ATLAS is based on combining the output of three separate *b*-tagging algorithm types: Impact Parameter based (IP2D and IP3D, described in Section 2.6.0.1), Secondary Vertex based (SV, described in Section 2.6.0.2) and Decay Chain based (JetFitter, described in Section 2.6.0.3) into a multivariate discriminant (MV2, covered in Section 2.6.1) which is used to distinguish the jet flavours. These algorithms have undergone continuous improvement over the Run-2 cycle of the LHC to improve the separation of jet flavours.

The inputs for each of the *b*-tagging algorithms are all taken from the ID of the ATLAS detector (Section 2.2.1). This limits *b*-tagging to jets with  $|\eta| < 2.5$ , and in addition jets with a  $p_T < 20\text{GeV}$  are not selected for *b*-tagging, nor jets determined to be likely a result of pileup in the detector which are eliminated using a multivariate discriminant, the Jet Vertex Tagger algorithm [34, 35].

#### 2.5.2.1 IP2D and IP3D: Impact Parameter based Algorithms

The typical topology of a *b*-hadron ; a secondary vertex displaced from the hard scatter interaction point as a results of the lifetime of *b*-quark, is used as the basis of these algorithms. Impact parameters of tracks from the secondary vertex are computed with respect to the primary vertex of the interaction. The IP2D algorithm uses a transverse impact parameter ( $d_0$ ) defined as the distance of closest approach of a track to the primary vertex in  $(r, \phi)$  plane around the vertex. The IP3D algorithm uses both the transverse and a correlated longitudinal impact parameter ( $z_0 \sin \theta$ ), defined as the distance between the point of closest approach in  $(r, \phi)$  and the primary vertex in the longitudinal plane. These parameters typically have large values as a result of the lifetime of *b*-quark. The signs of the impact parameters are also defined to take account of if they lie in front or behind the primary vertex with respect to the jet direction, with secondary vertices occurring behind the primary vertex normally due to background.

The significance of the impact parameter values ( $\frac{d_0}{\sigma_{d_0}}, \frac{z_0}{\sigma_{z_0 \sin \theta}}$ ) for each track are compared to probability density functions obtained from reference histograms derived from Monte Carlo simulation, with each track being compared to a selection of reference track categories. This results in weights which are combined using a log-likelihood ratio (LLR) discriminant to compute an overall jet weight separating the *b*, *c*, and light-jet flavours from each other. [35, 36]

#### 2.5.2.2 SV1: Secondary Vertex Finding algorithm

The secondary vertex algorithm uses the decay products of the *b*-hadron to reconstruct a distinct secondary vertex. The algorithm uses all tracks that are significantly displaced from the primary

vertex associated with the jet, forming vertex candidates for all pairs of track, while rejecting any vertices that would be associated with decay of long lived particles (e.g.  $\Lambda$ ,  $uds$ ), photon conversions or interactions with the material in the detector. The tracks forming these vertex candidates are then iteratively combined and refined to remove outliers beyond a  $\chi^2$  threshold leaving a single inclusive vertex.

The properties of this secondary vertex are used to differentiate the flavour of the jet. The SV1 algorithm is based on a LLR formalism similar to the IP algorithms, and makes use of the invariant mass of all charged tracks used to reconstruct the vertex, the number of two track vertices and the ratio of the invariant mass of the charged tracks to the invariant mass of all tracks. In addition the algorithm is signed in a similar fashion to the IP algorithms and uses the  $\Delta R$  between the jet direction and secondary vertex displacement direction in the LLR calculation. The algorithm uses distributions of these variables to distinguish between the jet flavours [35, 36].

### 2.5.2.3 JetFitter: Decay Chain Multi based Algorithm

The JetFitter algorithm exploits the topological structure of weak  $b$ -hadron and  $c$ -hadron decays inside the jet to reconstruct a full  $b$ -hadron decay chain. A Kalman filter is used to find a common line between the on which lie the  $b$ ,  $c$  and primary vertices to approximate the  $b$ -hadron flight path [37]. A selection of variables relating to the primary vertex and the properties of the tracks associated with the jet are used as input nodes in a neural network. This neural network uses the input variables,  $p_T$  and  $|\eta|$  variables from the jets, reweighted to ensure the spectra of the kinematics are not used in the training of the neural net. The neural network outputs discriminating variables relating to each jet flavour which are used to tag the jets. [?]

### 2.5.3 Multivariate Algorithm

The output variables of the three basic algorithms described prior are combined as input into the Multivariate Algorithm MV2. MV2 is a Boosted Decision Tree (BDT) algorithm which has been trained on  $t\bar{t}$  events to discriminate  $b$ -jets from light and  $c$ -jets. The algorithm makes use of the jet kinematics in addition to the tagger input variables to prevent the kinematic spectra of the training sample from being used as discriminating factor. The MV2 algorithm is an revised version of the MV1 algorithm used during Run-1 of the LHC, and has three sub-variants (MV2c00, MV2c10, and MV2c20) of the algorithm distinguished by the exact background composition of the training sample. The naming convention initially referred to the  $c$ -jet composition of the training sample, e.g. for MV2c20 the  $b$ -jets are designated as signal jets where a mixture of 80% light jets and 20%  $c$ -jets was designated as background.

The MV2 algorithm has a set of working points, defined by a single value of the output distribution of the algorithm, which are configured to provide a specific  $b$ -jet selection efficiency on the training  $t\bar{t}$  sample. Rather than being used independently, physics analyses will make use of several working points as an increase in  $b$ -jet efficiency (corresponding to *looser*  $b$ -jet selection) will bring an increased mistag rate of light and  $c$ -jets .

These algorithms were refined prior to the 2016 Run-2 data-taking session in response to  $c$ -jets limiting physics analyses more the light-jets. This change to enhance the  $c$ -jet rejection meant that for the MV2c10, the  $c$ -jet fraction was set to 7% in training and the fraction for MV2c20 was 15%. There were a selection of other improvements made to the algorithm relating to the BDT training parameters and the use of the basic algorithms before the 2016 data taking. With these refinements, the MV2c10 algorithm was found to provide a comparable level of light-jet rejection to the original 2015 Mv2c20 algorithm with improved  $c$ -jet rejection, so was chosen as the standard  $b$ -tagging algorithm for 2016 analyses. [35]

## 2.6 Trigger-Object Level Analysis

In physics analyses at the LHC, the 1kHz event readout rate to storage is significantly below the 40MHz bunch crossing rate. This bottleneck is caused by the limited bandwidth (Event rate  $\times$  Event size in bytes) available to analysis channels. In searches with large backgrounds or those with low rates, the prescaling introduced in the trigger system critically effects the amount of significant events output to storage, limiting the statistical power of any search in these hard to isolate channels as a large number of events are discarded to keep output within bandwidth limitations.

This constraint can be alleviated by recording only a fraction of the detector readout for any given event, specifically the jet information reconstructed by the triggering system. This partial event corresponds to a reduction in the event size in bytes which allows for present bandwidth limitations to be upheld with an increased event rate. This process of using the objects produced in the trigger as substitutes for the offline objects is referred to as Trigger-Object Level Analysis (TLA) [38].

In these analyses, partially built events are collected using an additional TLA stream of the output data, which records the jet four-momentum along with a selection of additional identifying variables for jet objects in the HLT, triggered by jet objects from the L1 trigger. The readout does not include individual calorimeter cells nor information from the muon or tracking detectors, and in prior application of a TLA approach to a search for light dijet resonances [38] a partial TLA event was 5% of the size of a full detector readout.

## EVENT SELECTION

NOTES: what do we need in this section  
 L: xAODs offline recovery online recover central channels triggers used

### 3.1 Samples

Real event data was taken from the 2016 13 TeV run, with Data Period D used owing to limited storage space on analysis computing facilities. The analysis used the all year 25ns Good Runs List, `data16_13TeV.periodAllYear_DetStatus-v88-pro20-21_DQDefects-00-02-04_PHYS_StandardGRL_All_Go` resulting a data luminosity of  $36.1 \text{ fb}^{-1}$ . The simulated VBF sample used, `mc15_13TeV.341566.PowhegPyth` was produced during the MC15c production period. The sample uses the HIGG5D3 xAOD derivation as described in Ref. [?]. The sample was produced using the NLO generator POWHEG configured using the CTEQ6L1 [39] set of PDFs and interfaced with PYTHIA8 tuned to AZNLO [40].

#### 3.1.1 Event weights

In order to accurately compare the simulated events from the Monte-Carlo samples with the 2016 dataset, it is necessary to normalise the Monte-Carlo samples to the total luminosity of the dataset, based on the theoretical cross-section for the interaction. The Monte-Carlo simulation assigns a weight  $w_i$  to each event simulated, which are summed to give the total number of events in the Monte-Carlo. Each bin in results produced from the simulated data is reweighted using a scaling factor

$$w_{MC} = \frac{\sigma k L}{N} \quad (3.1)$$

where  $\sigma$  is the theoretical cross section,  $L$  the integrated luminosity of the real dataset,  $N$  the total number of simulated events ( $\sum_N w_i$ ) and  $k$  the Real  $K$ -Factor, which is a correction to the leading order cross section to reproduce the higher order calculation for the interaction.

### 3.2 VBF $H \rightarrow b\bar{b}$ Analysis Strategy

As higgs bosons are colour singlets, there is no colour charge connection between the  $b$ -quarks produced in the interaction and the other final state particles, which leads to little hadronic activity and QCD radiation. This results in the two VBF jets being produced with a high rapidity gap, the pair of which along with the central  $b$ -jets form the characteristic final state for the interaction. With this in mind, the VBF  $H \rightarrow b\bar{b}$  events are separated from the high QCD multijet background by requiring two central  $b$ -jets which form the higgs candidate and two high  $p_T$  non  $b$ -tagged VBF jets. The analysis is split into two separate channels, related to details of the topology and the trigger chains used. The *four-central* channel requires all four jets to be contained within the central region  $|\eta| < 2.8$  and the *two-central* channel requires two jets in the central region and one forward jet. In this study, the online trigger level jets could not be extracted for the *four-central* trigger chains, so analysis focusses on the *two-central* channel.

To do: cite 2017  
vbfhbb paper

For the *two-central* channel, the event was required to pass the HLT\_j80\_bmv2c2070\_split\_j60\_bmv2c2085\_split trigger. The event was required to contain one jet with  $p_T > 95\text{GeV}$  which was  $b$ -tagged at the *tight* working point and one additional jet with  $p_T > 70\text{GeV}$  that passed the *loose*  $b$ -tagging working point. One forward jet with  $3.2 < |\eta| < 4.4$  and  $p_T > 60\text{GeV}$  was required along with a final VBF jet with  $p_T > 20\text{GeV}$  and  $|\eta| < 4.4$ . Finally the  $p_T$  of the  $b\bar{b}$  pair was required to exceed  $160\text{ GeV}$ . (This is to remove sculpting EXPLAINNNN)

### 3.3 Jet Extraction

The analysis is based on the jet objects reconstructed from the detector contained in the DxAOD. Both the offline jet objects and the online equivalents are retrieved, however the method by which the full collection of jets is assembled differs between each case. For offline jet objects, the DxAOD contains a complete set of jets for each reconstruction algorithm, which are each associated to the relevant jet  $b$ -tagging information.

In selecting the trigger level offline jets, firstly all *split-jets* that pass the trigger are retrieved from the trigger chain. Any duplicates, determined through  $\Delta R$  matching, are removed and the  $b$ -tagging information is associated with the jets. Following this all L1 trigger jets are retrieved,

which do not possess  $b$ -tagging information. The full set of L1 jets is compared to the *split-jets* and any duplicates are removed from the HLT jet set to form the *nonsplit-jets*. The combination of the *split-jets* and *nonsplit-jets* forms the complete jet collection for the trigger level event.

### 3.4 Jet Assignment

For both online and offline studies the jet collections are processed to extract the four VBF  $H \rightarrow b\bar{b}$  jets. Firstly separate collections of jets that pass the *loose*  $b$ -tagging working point and lower  $b$ -jet  $p_T$  cut and jets that do not pass the  $b$ -tagging but pass the lower VBF jet cut are assembled.

This section describes the selection criteria required for the events and reconstructed objects used in the analysis. These cuts and criteria are designed with the VBF  $H \rightarrow b\bar{b}$  event topology in mind, along with the limitations introduced by considering the available trigger chains as discussed in Section ???. These cuts are applied in the VBF  $H \rightarrow b\bar{b}$  analysis and the direct object comparison covered in Chapter 4.

### 3.5 Events

Data events were required to pass the all year 25ns Good Runs List<sup>a</sup> ??? and also be Clean ???.

### 3.6 Offline Jets

Offline jet reconstruction was performed by the anti- $k_t$  algorithm ( $R=0.4$ ) as discussed in Section ???. Jets were calibrated in line with the 20.7 recommendations ???. When considering individual jets during the analysis, all jets were required to have a  $p_T > 45$  GeV to be recorded.

### 3.7 Online Jets

Online Jet reconstruction is a mystery. A full collection of online jets was recovered by extracting the split jets (Section

### 3.8 Offline $b$ -jets

The specifics of  $b$ -tagging are covered in Section 2.6. Offline  $b$ -jets were tagged using the *MV2c10*-tagger<sup>b</sup> with two defined efficiency working points: *Tight*, with an overall efficiency

<sup>a</sup>data16\_13TeV.periodAllYear\_DetStatus-v88-pro20-21\_DQDefects-00-02-04\_PHYS\_StandardGRL\_All\_Good\_25ns.xml

<sup>b</sup>Jan 2017 Recommendations: 2016-20\_7-13TeV-MC15-CDI-2017-01-31\_v1.root

of 70% and *Loose* with 85% tagging efficiency.

### 3.9 Online $b$ -jets

Online  $b$ -jets were tagged using the  $MV2c20$ -tagger<sup>c</sup> with two defined efficiency working points: *Tight*, with an overall efficiency of 70% and *Loose* with 85% tagging efficiency.

---

<sup>c</sup>Mar 2016 Recommendations: 2016-Winter-13TeV-MC15-CDI-March10\_v1.root

## OBJECT PERFORMANCE

Prior to conducting a full study of TLA on the VBF  $H \rightarrow b\bar{b}$  channel, the features of jet objects reconstructed offline and within the HLT were compared to identify any performance differences in the base components of an event reconstruction. The jet objects were compared on a one to one basis, by matching an online jet to an offline jet by requiring the  $\Delta R$  value between the two jets to be below a threshold value of 0.3<sup>a</sup>.

**To do:** Does this need a plot, or is this sufficient?

To compare the online and offline jets, the ratio of the difference in value for (significant) jet properties between the matched jets were evaluated. These values were calculated for jet feature  $X$  using:

$$\Delta X_{ratio} = \frac{X_{Offline} - X_{Online}}{X_{Offline}} \quad (4.1)$$

where  $X_{Offline}$  is the value of the feature on the offline jet, and  $X_{Online}$  is from the HLT jet. Specific categories of jets within the event were compared to ensure the most relevant jets for the analysis were comparable.

The performance of the online and offline jet features was tested bearing in mind the final state products of the VBF  $H \rightarrow b\bar{b}$  interaction, while considering the rapidity of the produced jets.

---

<sup>a</sup>Determined from a plot of  $\Delta R$  values between all pairs of jets



## 4.1 Leading $b$ -jets

The leading  $p_T$  offline  $b$ -jet was selected from the event, requiring the jet to pass the *Tight*  $b$ -tagging working point. This jet was matched to a corresponding online jet using  $\Delta R$  matching, and the properties of each of these jets compared in both Data and Monte-Carlo.

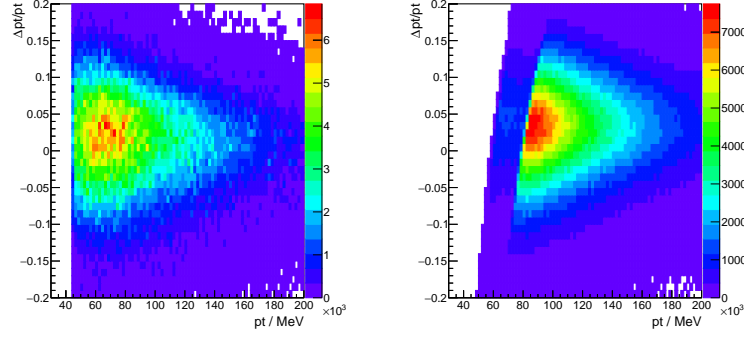


**Figure 4.1:**  $\Delta p_T$  ratio for the leading  $p_T$   $b$ -jet against  $p_T$  of the offline  $b$ -jet, plotted for Monte-Carlo simulated results (left) and real data (right).

The comparative performance of the online and offline jets is  $p_T$  is broadly similar for events in both Data and Monte-Carlo. The bulk of the results occur with a  $\Delta p_T$  ratio  $\sim 0$  and the two plots show a comparable drop off in  $p_T$  distribution. The distinctive curve present in the results from the Data is an artefact of the trigger used in real data, which is not required for the Monte-Carlo. As discussed in , the real Data was required to pass a trigger with at least one jet with a  $p_T > 80\text{GeV}$  which results in the steep drop-off below this cut value.

To do: make this point

The distribution of the  $\Delta p_T$  ratio about 0 can be shown by taking a slice across the distribution for a representative  $p_T$  value. The  $\Delta p_T$  ratio values were also split into  $\eta$  bands to study performance at different points in the detector. For the leading  $b$ -jet, this is constrained to be within the region of the detector (Section ??) where  $b$ -tagging is available.

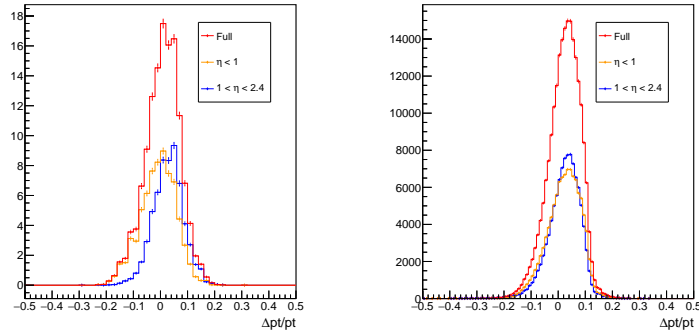


**Figure 4.2:**  $\Delta p_T$  ratio distribution for the leading  $b$ -jet with  $89 < p_T < 91$  GeV. The distributions for all events and events split by  $\eta$  region are shown.

The results show similar profiles between the Monte-Carlo and Data events for  $\Delta p_{\text{T } ratio}$ . Both plots show the offline  $p_{\text{T}}$  values to be consistently higher than the online, with a median shift of 4% in Data and 2% in Monte-Carlo. The performance between  $\eta$  ranges was also consistent. The profiles broadly match the full shape and each other, but the Monte-Carlo showed a slight difference in  $\Delta p_{\text{T } ratio}$  value as the central  $\eta$  range peaked at  $\sim 0$ . The breadth of these distributions is quite large, with both Data and Monte-Carlo showing  $\pm 10\%$  in  $\Delta p_{\text{T } ratio}$ .

These comparisons can be carried out for other jet properties (e.g.  $\eta$ ,  $\phi$ ) to confirm the offline and online jets are behaving in a similar fashion.

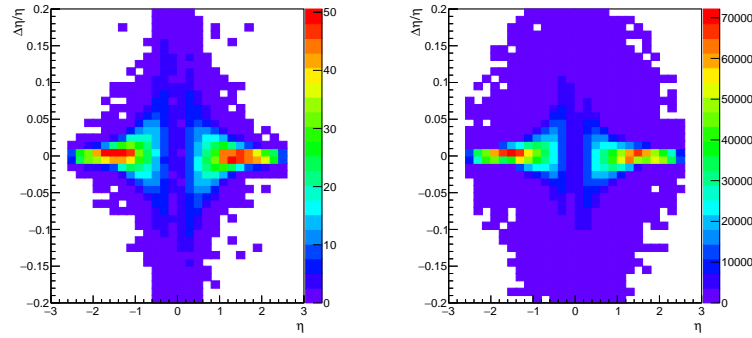


**Figure 4.3:**  $\Delta\eta_{ratio}$  for the leading  $b$ -jet, for Monte-Carlo events (left) and real data (right).

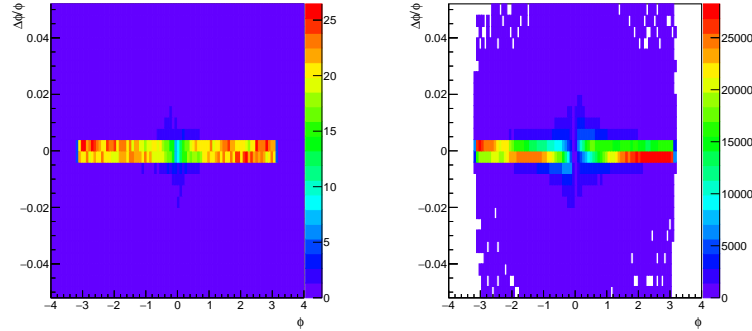


**Figure 4.4:**  $\Delta\phi_{ratio}$  for the leading  $b$ -jet, for Monte-Carlo events (left) and real data (right).

The Data and Monte-Carlo distributions for these values are extremely similar to each other, and also show very close agreement between the values for offline and online jet objects. In both cases the median  $\Delta X_{ratio}$  value is  $\sim 0$  and the breadth of the distribution is less than 1% of the value.

## 4.2 Leading Non $b$ -jets

For VBF  $H \rightarrow b\bar{b}$  the pair of high  $p_T$  forward jets is the other significant feature, so the offline/online performance in the leading Non  $b$ -jet was studied.

**To do:** Do we require this to fail the btagging

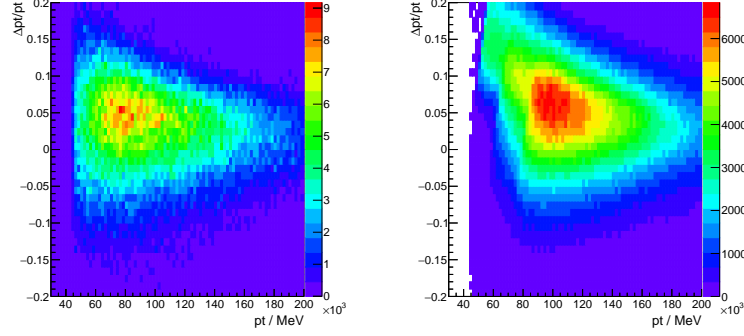


**Figure 4.5:**  $\Delta p_T$  ratio for the leading  $p_T$  non  $b$ -jet against  $p_T$  of the offline jet, plotted for Monte-Carlo simulated results (left) and real data (right).

The leading non  $b$ -jet shows a similar situation to the leading  $b$ -jet. At the peak of the  $\Delta p_T$  ratio distribution the  $p_T$  of the offline jet is within 5% of the online  $p_T$ , and the overall shape of the distribution is comparable between the Monte-Carlo and real Data events. As with the  $b$ -jets, the trigger in the real data required a jet in the forward region with  $p_T > 45$  GeV.

The results could also be split across  $\eta$  regions, with the added ability to study the forward regions of the detector.

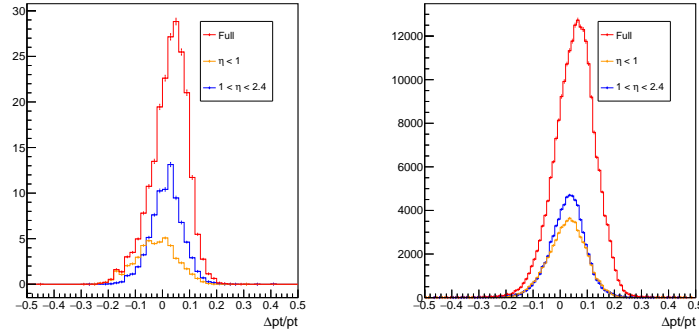


**Figure 4.6:**  $\Delta p_T$  ratio distribution for the leading non  $b$ -jet with  $89 < p_T < 91$  GeV. The distributions for all events and events split by  $\eta$  region are shown.

Both Monte-Carlo and Data show offline jets to be consistently higher  $p_T$  than online by 4% and 6% respectively. The overall distribution shape is similar between the simulated and real events, and the shape of the distributions for each  $\eta$  band is also comparable. Both the MC

and the Data show that the offset in  $p_T$  value is worse for the jets in the forward region than in the central regions of the detector, with a significantly higher median  $\Delta p_T$  ratio.

The other topological variables can also be compared.

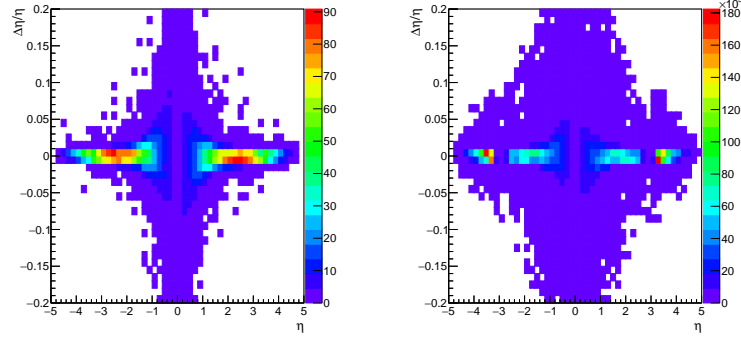


**Figure 4.7:**  $\Delta\eta_{ratio}$  for the leading non  $b$ -jet , for Monte-Carlo events (left) and real data (right).

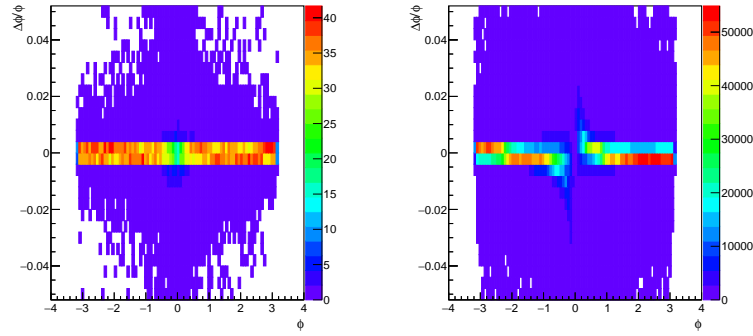


**Figure 4.8:**  $\Delta\phi_{ratio}$  for the leading non  $b$ -jet , for Monte-Carlo events (left) and real data (right)

As with the  $b$ -jets , for these other variables offline and online jets produce nearly identical results, with the distribution of  $\Delta X_{ratio}$  firmly centred around 0 and a breadth of less than 1%.

#### 4.2.1 Comparison of Jet Objects between Offline and Online

The jet objects reconstructed in the HLT have some slight differences in the reported values for key topological variables, but overall they perform in a similar fashion, both in Monte-Carlo simulations and in Real data. The positional variables,  $\phi$  and  $\eta$  are directly comparable between offline and online jet objects, with the majority of objects having values with  $< 1\%$  disagreement for both  $b$ -jets and non  $b$ -jets . For the  $p_T$  of jet objects, the values are not in perfect agreement, but have a consistent offset observed in Monte-Carlo and Real data which could be overcome with specific calibration of the jet objects reconstructed in the HLT.

### 4.3 Jet Tagging Efficiency

As covered in 2.6.1, the standard algorithm for 2016 physics analyses was chosen to be the 2016 MV2c10 algorithm. However, the HLT  $b$ -tagging algorithm uses the MV2c20 algorithm. [30] To perform a valid TLA the performance of the tagging algorithms between trigger level and offline must be similar. With the datasets used for this analysis (??) the MC data produced in 2015 would make use of the older configurations compared to the newer configurations in the data.

Here the tagging efficiency of the HLT and offline taggers is studied for different jet flavours in the MC sample. An offline/HLT jet pair was formed using  $\Delta R$  matching and truth label of the jet used to assign a flavour. The efficiency plots in figures 4.9, 4.10 and 4.11 show the fraction of these jets that were identified as  $b$ -jets by the HLT and offline tagging algorithms.

The jet objects reconstructed online and offline contain the  $b$ -tagging decision for that object. In the Monte-Carlo xAOD data, the truth label of a jet could be used to determine the exact nature of the jet. The  $b$ -tagging decision of jets truth labelled as  $b$ -jets,  $c$ -jets and light-jets was studied for both offline and online to compare the efficiency of the algorithms.

not sure what effect  
this config changes  
had on the trigger

#### 4.3.1 $b$ -jet efficiency

For jets labelled as true  $b$ -jets, the tagging efficiency can be calculated and plotted with respect to topological variables of the jet objects.

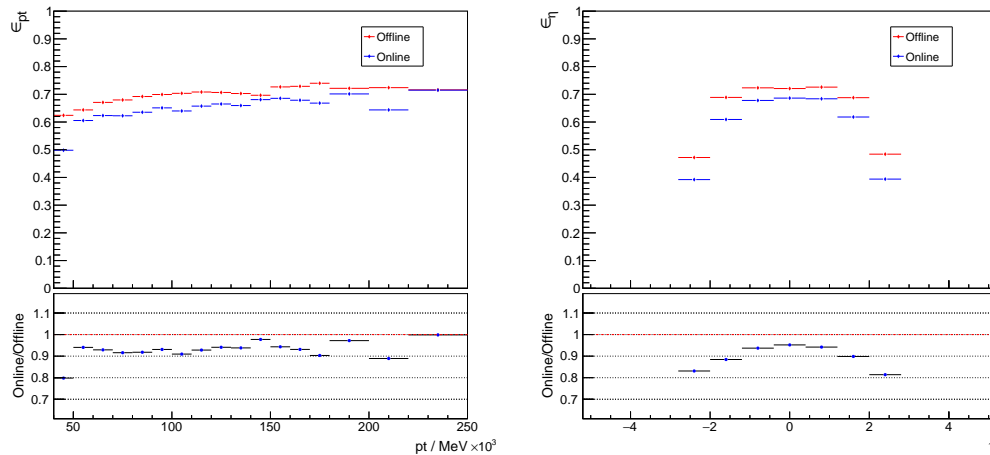


**Figure 4.9:**  $b$ -tagging efficiency for truth  $b$ -jets in Monte-Carlo data, plotted against jet  $p_T$  (left) and  $\eta$  (right). Analysis is confined to the central region of the detector where  $b$ -tagging is operational.

**To do:** Options,  
could show more  
vars or alternatively  
the reference hists,  
or alternatively just  
reference the  
references

### 4.3.2 $c$ -jet efficiency

For  $c$ -jets and light-jets, plotting the same value gives the mistag rate for these jets in the detector.

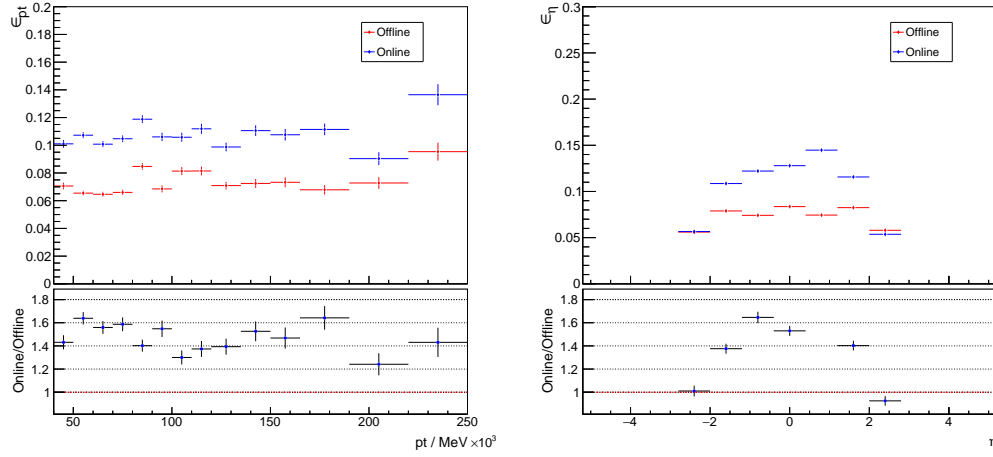


**Figure 4.10:** Mistag rate for truth  $b$ -jets in Monte-Carlo data, plotted against jet  $p_T$  (left) and  $\eta$  (right). Analysis is confined to the central region of the detector where  $b$ -tagging is operational.

### 4.3.3 Light-jet efficiency

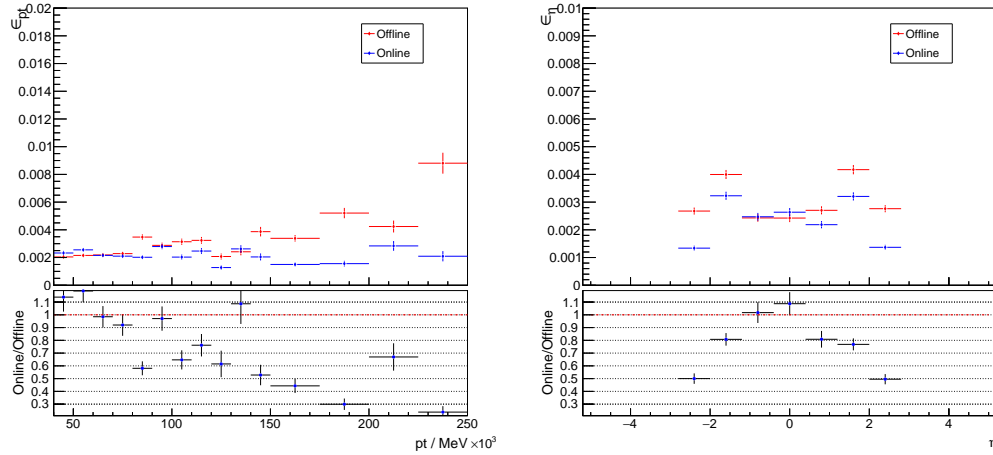


**Figure 4.11:** Mistag rate for truth light-jets in Monte-Carlo data, plotted against jet  $p_T$  (left) and  $\eta$  (right). Analysis is confined to the central region of the detector where  $b$ -tagging is operational.

#### 4.3.4 Tag Matching

For each pair of jets that could be matched between online and offline, and then successfully have a  $b$ -tagging decision evaluated on the jets, the agreement of the  $b$ -tagging between the two jets was checked. These were found to match one another in 91% of cases.

#### 4.3.5 Comparison of HLT and offline tagging efficiencies

Primarily considering the  $p_T$  plots of efficiency, the HLT  $b$ -tagging is found to be around 5% less efficient than the offline  $b$ -tagging for jets with  $p_T > 50\text{GeV}$ . This is a consistent direction of efficiency shift as found when comparing the 2016 MV2c10 and 2015 MV2c20 algorithms on the training  $t\bar{t}$  sample, but of a larger magnitude. The increase in the rate of  $c$ -jet mistagging is absolutely consistent with the refinements to the algorithm between the 2016 MV2c10 and 2015 MV2c20, with increased levels of  $c$ -jet rejection in the offline 2016 MV2c10, and the  $\sim 40\%$  increase is consistent with the expected shift from the optimised algorithm. [35] The light-jet behaviour is also similar as expected but ????

To do: some light  
jet related  
shenanigans

## KINEMATICS

## 5.1 Specific Jet Feature Distributions

In events that pass sufficient selection cuts to be considered candidates for a VBF  $H \rightarrow b\bar{b}$  event, the specific jet features for the 4 candidate jets can be compared for offline and online.

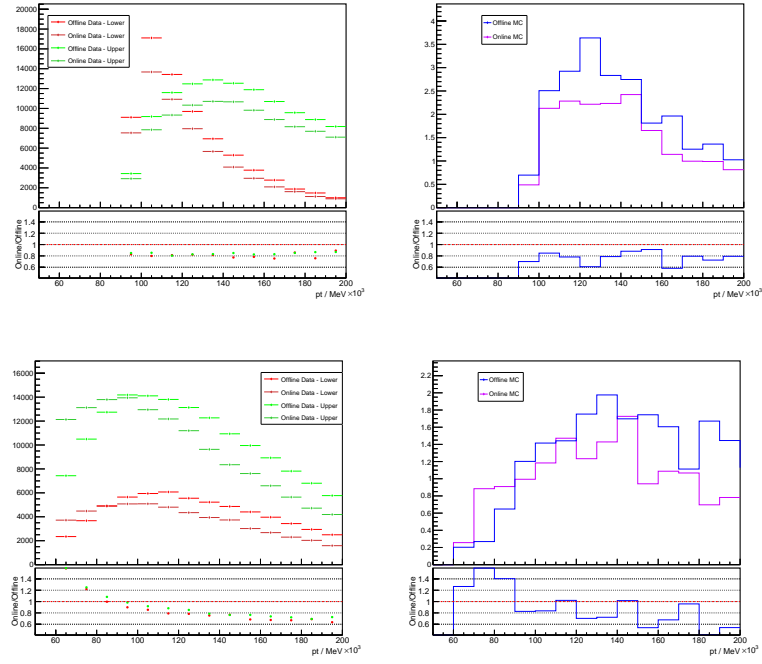
### 5.1.0.1 $p_T$

### 5.1.0.2 $\eta$

## 5.2 BDT Input Variables

- $M_{jj}$
- $p_{T\ jj}$
- $\cos \theta$
- $\Delta\eta_{jj}$
- $Max(\eta)$
- $\eta^*$
- $min\Delta R(j_1)$
- $min\Delta R(j_1)$
- $p_T$  balance
- $N_{TRK}(j_1)PV500$  ?
- $N_{TRK}(j)PV500$  ?





### 5.3 Mbb Distribution

Prior paper suggests this is the 'final' plot, a shape comparison between BDT influenced control and signal regions of the  $M_{bb}$  distribution. A little confused as to exactly what we need here.

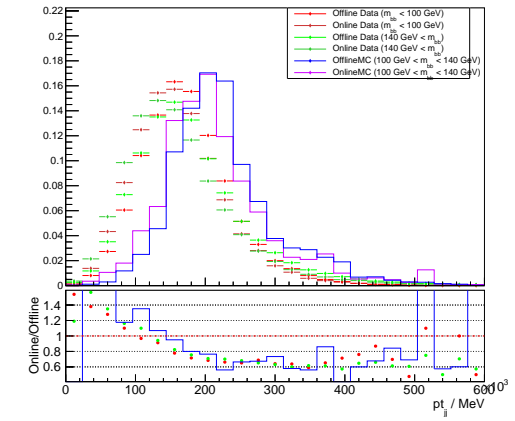
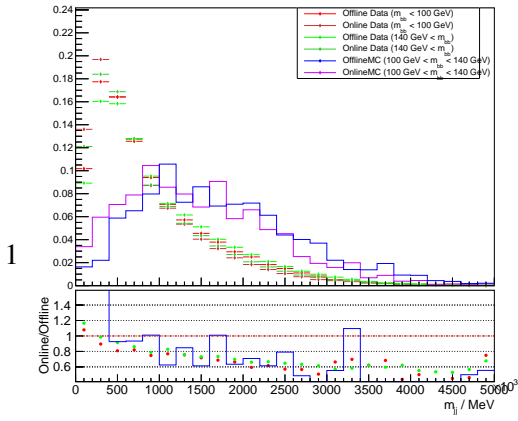
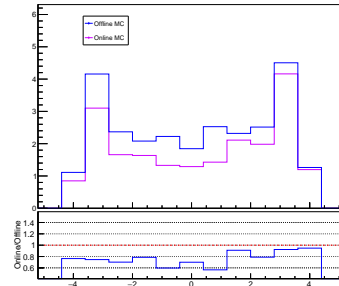
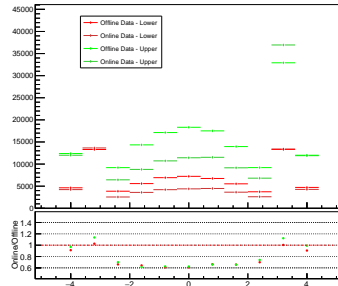
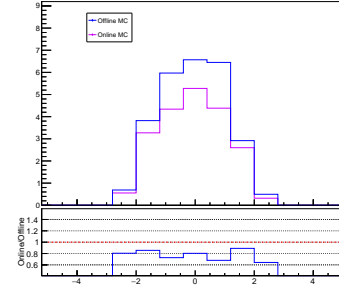
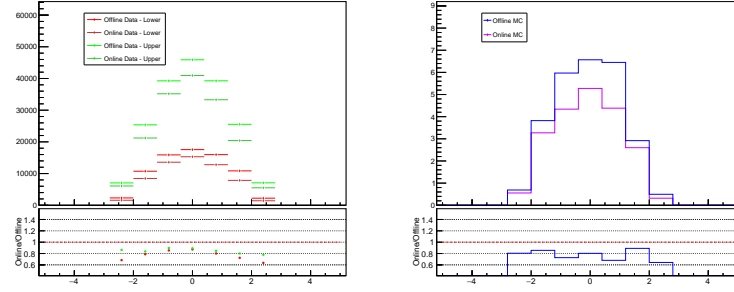


Figure 5.1:

Figure 5.2:

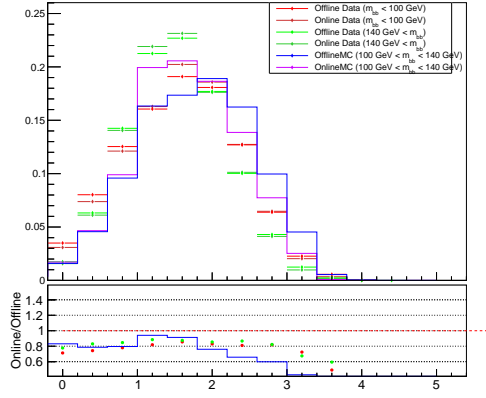


Figure 5.3:

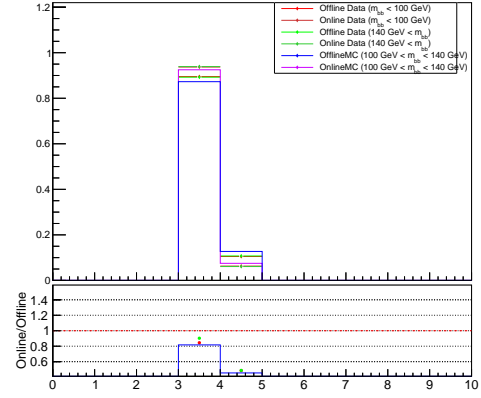


Figure 5.4:

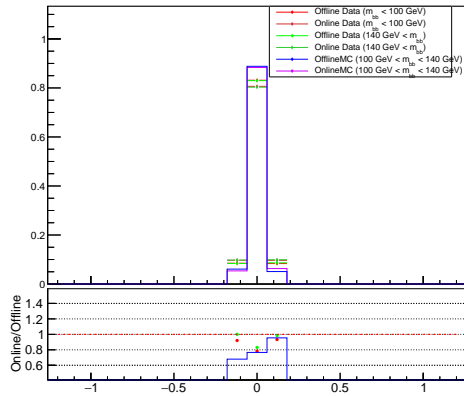


Figure 5.5:

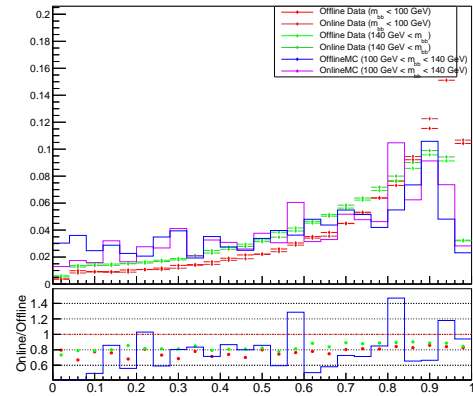


Figure 5.6:

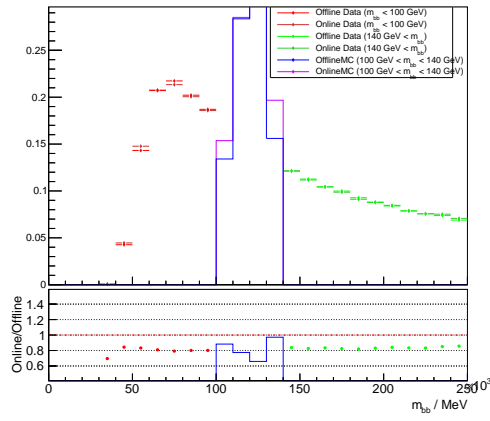


Figure 5.7:

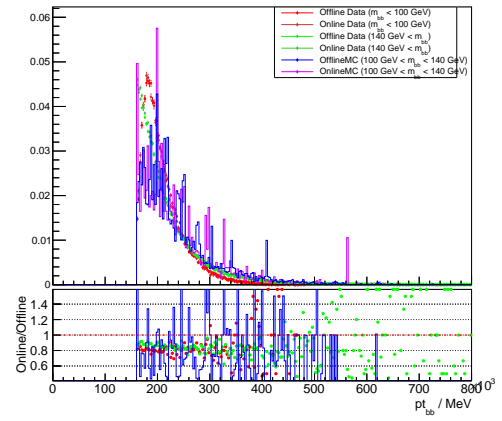


Figure 5.8:

## BIBLIOGRAPHY

- [1] Particle Data Group Collaboration, C. Patrignani et al., *Review of Particle Physics*, [Chin. Phys. C](#) **40** no. 10, (2016) 100001.
- [2] F. Englert and R. Brout, *Broken Symmetry and the Mass of Gauge Vector Mesons*, [Phys. Rev. Lett.](#) **13** (1964) 321–323.
- [3] P. W. Higgs, *Broken Symmetries and the Masses of Gauge Bosons*, [Phys. Rev. Lett.](#) **13** (1964) 508–509.
- [4] P. W. Higgs, *Broken symmetries, massless particles and gauge fields*, [Phys. Lett.](#) **12** (1964) 132–133.
- [5] S. L. Glashow, *Partial Symmetries of Weak Interactions*, [Nucl. Phys.](#) **22** (1961) 579–588.
- [6] S. Weinberg, *A Model of Leptons*, [Phys. Rev. Lett.](#) **19** (1967) 1264–1266.
- [7] A. Salam, *Weak and Electromagnetic Interactions*, Conf. Proc. **C680519** (1968) 367–377.
- [8] N. Cabibbo, *Unitary Symmetry and Leptonic Decays*, [Phys. Rev. Lett.](#) **10** (1963) 531–533. [,648(1963)].
- [9] M. Kobayashi and T. Maskawa, *CP Violation in the Renormalizable Theory of Weak Interaction*, [Prog. Theor. Phys.](#) **49** (1973) 652–657.
- [10] ATLAS Collaboration, G. Aad et al., *Observation of a new particle in the search for the Standard Model Higgs boson with the ATLAS detector at the LHC*, [Phys. Lett. B](#) **716** (2012) 1–29, [arXiv:1207.7214 \[hep-ex\]](#).
- [11] CMS Collaboration, S. Chatrchyan et al., *Observation of a new boson at a mass of 125 GeV with the CMS experiment at the LHC*, [Phys. Lett. B](#) **716** (2012) 30–61, [arXiv:1207.7235 \[hep-ex\]](#).
- [12] NNPDF Collaboration, R. D. Ball et al., *Parton distributions for the LHC Run II*, [JHEP](#) **04** (2015) 040, [arXiv:1410.8849 \[hep-ph\]](#).
- [13] J. C. Collins, *Light cone variables, rapidity and all that*, [arXiv:hep-ph/9705393 \[hep-ph\]](#).

- [14] M. H. Seymour and M. Marx, *Monte Carlo Event Generators*, pp. , 287–319. 2013.  
[arXiv:1304.6677 \[hep-ph\]](#).  
<https://inspirehep.net/record/1229804/files/arXiv:1304.6677.pdf>.
- [15] B. Andersson, G. Gustafson, G. Ingelman, and T. Sjöstrand, *Parton fragmentation and string dynamics*, *Physics Reports* **97** no. 2, (1983) 31 – 145.  
<http://www.sciencedirect.com/science/article/pii/0370157383900807>.
- [16] B. R. Webber, *A QCD Model for Jet Fragmentation Including Soft Gluon Interference*, *Nucl. Phys.* **B238** (1984) 492–528.
- [17] T. Sjöstrand, S. Ask, J. R. Christiansen, R. Corke, N. Desai, P. Ilten, S. Mrenna, S. Prestel, C. O. Rasmussen, and P. Z. Skands, *An Introduction to PYTHIA 8.2*, *Comput. Phys. Commun.* **191** (2015) 159–177, [arXiv:1410.3012 \[hep-ph\]](#).
- [18] T. Gleisberg, S. Hoeche, F. Krauss, M. Schonherr, S. Schumann, F. Siegert, and J. Winter, *Event generation with SHERPA 1.1*, *JHEP* **02** (2009) 007, [arXiv:0811.4622 \[hep-ph\]](#).
- [19] C. Oleari, *The POWHEG-BOX*, *Nucl. Phys. Proc. Suppl.* **205-206** (2010) 36–41, [arXiv:1007.3893 \[hep-ph\]](#).
- [20] LHC Higgs Cross Section Working Group Collaboration, S. Dittmaier et al., *Handbook of LHC Higgs Cross Sections: 1. Inclusive Observables*, [arXiv:1101.0593 \[hep-ph\]](#).
- [21] S. Asai et al., *Prospects for the search for a standard model Higgs boson in ATLAS using vector boson fusion*, *Eur. Phys. J.* **C32S2** (2004) 19–54, [arXiv:hep-ph/0402254 \[hep-ph\]](#).
- [22] LHC Higgs Cross Section Working Group Collaboration, J. R. Andersen et al., *Handbook of LHC Higgs Cross Sections: 3. Higgs Properties*, [arXiv:1307.1347 \[hep-ph\]](#).
- [23] L. Evans and P. Bryant, *LHC Machine*, *JINST* **3** (2008) S08001.
- [24] *LEP design report*. CERN, Geneva, 1983. <https://cds.cern.ch/record/98881>. By the LEP Injector Study Group.
- [25] *LEP design report*. CERN, Geneva, 1984. <https://cds.cern.ch/record/102083>. Copies shelved as reports in LEP, PS and SPS libraries.
- [26] Y. Koshiba et al., *Luminosity Increase in Laser-Compton Scattering by Crab Crossing Method*, in *Proc. of International Particle Accelerator Conference (IPAC'17)*, Copenhagen, Denmark, 14–19 May, 2017, pp. , 902–904. JACoW, Geneva, Switzerland, May, 2017. <http://jacow.org/ipac2017/papers/mopva023.pdf>.  
<https://doi.org/10.18429/JACoW-IPAC2017-MOPVA023>.

- [27] ATLAS Collaboration, G. Aad et al., *The ATLAS Experiment at the CERN Large Hadron Collider*, **JINST** **3** (2008) S08003.
- [28] J. Pequeno, “Computer generated image of the whole ATLAS detector.” <https://cds.cern.ch/record/1095924>. Accessed 03/09/2017.
- [29] ATLAS Collaboration, M. zur Nedden, *The Run-2 ATLAS Trigger System: Design, Performance and Plan*, Tech. Rep. ATL-DAQ-PROC-2016-039, CERN, Geneva, Dec, 2016. <https://cds.cern.ch/record/2238679>.
- [30] ATLAS Collaboration, M. Aaboud et al., *Performance of the ATLAS Trigger System in 2015*, **Eur. Phys. J. C** **77** no. 5, (2017) 317, [arXiv:1611.09661](https://arxiv.org/abs/1611.09661) [hep-ex].
- [31] R. Achenbach et al., *The ATLAS level-1 calorimeter trigger*, **JINST** **3** (2008) P03001.
- [32] R. Atkin, *Review of jet reconstruction algorithms*, **J. Phys. Conf. Ser.** **645** no. 1, (2015) 012008.
- [33] M. Cacciari, G. P. Salam, and G. Soyez, *The Anti- $k(t)$  jet clustering algorithm*, **JHEP** **04** (2008) 063, [arXiv:0802.1189](https://arxiv.org/abs/0802.1189) [hep-ph].
- [34] *Tagging and suppression of pileup jets with the ATLAS detector*, Tech. Rep. ATLAS-CONF-2014-018, CERN, Geneva, May, 2014. <https://cds.cern.ch/record/1700870>.
- [35] ATLAS Collaboration, *Optimisation of the ATLAS  $b$ -tagging performance for the 2016 LHC Run*, ATL-PHYS-PUB-2016-012 (2016). <https://cds.cern.ch/record/2160731>.
- [36] ATLAS Collaboration, *Performance of  $b$ -Jet Identification in the ATLAS Experiment*, **JINST** **11** no. 04, (2016) P04008, [arXiv:1512.01094](https://arxiv.org/abs/1512.01094) [hep-ex].
- [37] R. Fruhwirth, *Application of Kalman filtering to track and vertex fitting*, **Nucl. Instrum. Meth. A** **262** (1987) 444–450.
- [38] ATLAS Collaboration, T. A. collaboration, *Search for light dijet resonances with the ATLAS detector using a Trigger-Level Analysis in LHC  $pp$  collisions at  $\sqrt{s} = 13$  TeV.*
- [39] J. Pumplin, D. R. Stump, J. Huston, H. L. Lai, P. M. Nadolsky, and W. K. Tung, *New generation of parton distributions with uncertainties from global QCD analysis*, **JHEP** **07** (2002) 012, [arXiv:hep-ph/0201195](https://arxiv.org/abs/hep-ph/0201195) [hep-ph].
- [40] ATLAS Collaboration, G. Aad et al., *Measurement of the  $Z/\gamma^*$  boson transverse momentum distribution in  $pp$  collisions at  $\sqrt{s} = 7$  TeV with the ATLAS detector*, **JHEP** **09** (2014) 145, [arXiv:1406.3660](https://arxiv.org/abs/1406.3660) [hep-ex].